RESEARCH ARTICLE

Key Points:
- Nucleation process of laboratory earthquakes is quantitatively reproduced by relatively simple, rate-and-state fault model
- Critical nucleation length and breakdown power density control the scaling of nucleating ruptures in laboratory experiments
- Loading rate or configuration significantly affects the propagation speeds of slow rupture front

Correspondence to:
Y. Kaneko,
y.kaneko@gns.cri.nz

The onset of laboratory earthquakes explained by nucleating rupture on a rate-and-state fault

Yoshihiro Kaneko[1], Stefan B. Nielsen[2], and Brett M. Carpenter[3,4]

[1]GNS Science, Lower Hutt, New Zealand, [2]Department of Earth Sciences, Durham University, Durham, UK, [3]School of Geology and Geophysics, University of Oklahoma, Norman, Oklahoma, USA, [4]Istituto Nazionale di Geofisica e Vulcanologia, Rome, Italy

Abstract

Precursory aseismic slip lasting days to months prior to the initiation of earthquakes has been inferred from seismological observations. Similar precursory slip phenomena have also been observed in laboratory studies of shear rupture nucleation on frictional interfaces. However, the mechanisms that govern rupture nucleation, even in idealized laboratory settings, have been widely debated. Here we show that a numerical model incorporating rate-and-state friction laws and elastic continuum can reproduce the behaviors of rupture nucleation seen in laboratory experiments. In particular, we find that both in laboratory experiments and simulations with a wide range of normal stresses, the nucleation consists of two distinct phases: initial slow propagation phase and faster acceleration phase, both of which are likely aseismic processes, followed by dynamic rupture propagation that radiates seismic waves. The distance at which the rupture transitions from the initial slow phase to the acceleration phase can be roughly predicted by a theoretical estimate of critical nucleation length. Our results further show that the critical nucleation length depends on the background loading rate. In addition, our analysis suggests that critical nucleation length and breakdown power derived from the Griffith crack energy balance control the scaling of nucleating ruptures. Moreover, the background loading rate and loading configuration significantly affect the rupture propagation speed. Furthermore, if the same nucleation mechanism applies to natural faults, the migration speed of foreshocks triggered by the propagation of slow rupture within the nucleation zone would depend on the effective normal stress and hence fluid pressure in the fault zone.

1. Introduction

The processes governing rupture initiation on frictional interfaces are key to understanding the nucleation of crustal earthquakes. Laboratory experiments [e.g., *Dieterich*, 1979; *Ruina*, 1983; *Ohnaka and Kuwahara*, 1990; *Kato et al.*, 1992; *Ohnaka*, 1996; *McLaskey and Kilgore*, 2013] and theoretical studies [e.g., *Okubo and Dieterich*, 1984; *Dieterich*, 1992; *Tullis*, 1996; *Lapusta and Rice*, 2003; *Rubin and Ampuero*, 2005; *Kaneko and Lapusta*, 2008; *Fang et al.*, 2010; *Schmitt et al.*, 2011; *Noda et al.*, 2013] suggest that earthquake faulting does not begin abruptly with dynamic rupture propagation but instead with accelerating aseismic rupture growth over a region of finite size called the nucleation zone. Although direct observation of slow rupture growth in the nucleation zone for a crustal earthquake remains difficult, seismological observations suggest that aseismic nucleation precedes the onset of some earthquake ruptures, which eventually radiate seismic waves. For example, analyses of well-recorded seismicity [e.g., *McGuire et al.*, 2005; *Dodge et al.*, 1996; *Bouchon et al.*, 2011; *Tape et al.*, 2013; *Schurr et al.*, 2014; *Yabe et al.*, 2015] imply that foreshocks are caused by the breaking of small-scale asperities on the fault, triggered by the propagation of aseismic slip in a region near the eventual hypocenter of the main shock. Understanding the mechanism of rupture nucleation is critical for the development of short-term earthquake prediction capabilities as it determines under what conditions detectable precursory signals may be generated.

From laboratory studies of shear rupture evolution on a frictional interface [e.g., *Ohnaka and Kuwahara*, 1990; *Kato et al.*, 1992; *Ohnaka*, 1996], the nucleation process can be qualitatively understood as the onset of a stick-slip frictional instability, which is characterized by a transition from slow rupture growth to accelerating fast rupture. However, a quantitative description of nucleation processes, even in idealized laboratory settings,
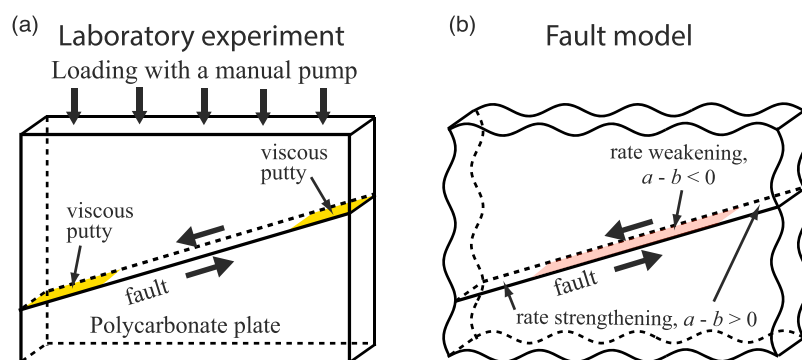
Figure 1. Schematic diagrams illustrating the setup of (a) laboratory experiments [*Latour et al.*, 2013] and (b) our numerical model.

is lacking due to difficulties in monitoring the transition of rupture behavior and explaining the laboratory observations using a realistic physical model.

Recent technological advances have made the accurate monitoring of nucleation processes in laboratory experiments possible. High-resolution photoelastic techniques have been used to image rupture growth and propagation on the frictional interface between two blocks of rock analogue materials [e.g., *Ben-David et al.*, 2010; *Nielsen et al.*, 2010; *Latour et al.*, 2013; *Svetlizky and Fineberg*, 2014]. In particular, the nucleation process of rapid shear slip events, in which the rupture gradually accelerates from a quasi-static slow speed to a fast dynamic rupture speed, has been reported [*Nielsen et al.*, 2010; *Latour et al.*, 2013]. In other studies [*Ben-David et al.*, 2010; *Svetlizky and Fineberg*, 2014] of frictional sliding with a different loading configuration, a wide range of slow to fast speeds for accelerating and decelerating ruptures has been observed, the origin of which is attributed to different ratios of local shear to normal stresses. However, there are a variety of views on how best to explain slow rupture propagation on a nominally flat frictional interface, ranging from a classical singular crack theory [*Svetlizky and Fineberg*, 2014], interactions between asperities represented by spring-slider network [*Trømborg et al.*, 2014], slip-weakening friction with [*Radiguet et al.*, 2015] or without [*Latour et al.*, 2013] bulk viscoelasticity, to rate-and-state friction [*Scholz*, 2002; *Kaneko and Ampuero*, 2011].

In this study, we analyze the nucleation processes of shear ruptures as observed in recent high-resolution photoelastic laboratory experiments [*Latour et al.*, 2013] using a fault model based on rate-and-state friction laws. We show, for the first time, that a continuum model incorporating rate-and-state friction quantitatively explains the spatial and temporal evolution of observed nucleating ruptures seen in laboratory experiments. We explore the behaviors of simulated nucleation processes with a range of friction parameters and loading conditions. We discuss the underlying mechanism of observed rupture nucleation and implications for the nucleation of crustal earthquakes.

2. Laboratory Observations of Shear Rupture Nucleation

In the laboratory experiments of *Latour et al.* [2013], vertical load was applied gradually to a polycarbonate slab with a planar fault cutting through the slab (Figure 1a). The process of spontaneous rupture nucleation on the interface was then monitored by acoustic sensors and high-speed photoelasticity, where the contrast of light intensity in the videograms was used to track the positions of the rupture tip during a sequence of stick-slip events [*Latour et al.*, 2013]. Several general and intriguing characteristics of rupture nucleation were observed in these experiments [*Latour et al.*, 2013]: (i) all the ruptures nucleated roughly at the same location and propagated in the same direction; (ii) rupture evolution occurred in three phases: initial slow quasi-static propagation, acceleration followed by rapid dynamic rupture propagation; (iii) the time and length scales of the quasi-static phase of rupture decreased with an increasing normal stress $\bar{\sigma}$, whereas the peak slip rate increased with $\bar{\sigma}$; and (iv) the period of rapid slip did not occur when $\bar{\sigma}$ was small (< 0.5 MPa).

3. Model Setup

To explain the nucleation behavior observed in these laboratory experiments, we simulated fault slip using a two-dimensional (2-D) in-plane elastodynamic model [*Lapusta and Liu*, 2009] in which rapid shear slip events (i.e., earthquakes) are modeled as part of a spontaneously occurring earthquake sequences on a fault

embedded into an infinite elastic medium. This approach allows us to study naturally developing stick-slip events, with conditions before the nucleation originating from the previous history of fault slip rather than from an arbitrarily selected prestress. Numerical simulations in this study were performed using a spectral boundary-integral method [*Lapusta and Liu*, 2009] where elastodynamic response of the medium is expressed as an integral relationship between stress and slip on the fault [*Geubelle and Rice*, 1995]. We use the numerical implementations of *Lapusta and Liu* [2009] and *Liu and Lapusta* [2008].

The fault constitutive response is represented by rate-and-state friction laws [*Dieterich*, 1979; *Ruina*, 1983]. In the framework of rate-and-state friction, frictional resistance τ of the fault is given by

$$\tau = (\sigma - p)\left[f_0 + a\ln\left(\frac{V}{V_0}\right) + b\ln\left(\frac{V_0\theta}{D_c}\right)\right],$$
$$\frac{d\theta}{dt} = -\left(\frac{V\theta}{D_c}\right)\ln\left(\frac{V\theta}{D_c}\right),$$

(1)

where σ is the normal stress, p is the pore pressure on the fault, $\sigma - p$ is the effective normal stress, a and b are rate-and-state constitutive parameters, V is slip rate, f_0 is the reference friction coefficient corresponding to the reference slip rate V_0, θ is a state variable which can be interpreted as the average age of the population of contacts between two surfaces, and D_c is the characteristic slip distance (i.e., the sliding distance required to renew the frictional contact population on the fault following a velocity step) [*Dieterich*, 1979; *Ruina*, 1983]. We assume the so-called "slip law" for the evolution of the state variable, which provides good fits to "velocity-jump" rock-friction experiments [*Ampuero and Rubin*, 2008; *Rathbun and Marone*, 2013]. The actual fault resistance to sliding in our model is given by rate-and-state friction regularized at zero slip velocity [*Lapusta and Liu*, 2009].

The setup of the fault model is motivated by and similar to that of the laboratory experiments [*Latour et al.*, 2013] (Figure 1a). The geometry, loading, and deformation in the experiments are essentially 2-D. To mimic this loading condition in our model, the fault is loaded by a background time-independent stressing rate $\dot{\tau}$ uniformly applied along the fault. The fault is divided up into three segments: a 14 cm long rate-weakening segment surrounded by 11 and 5 cm long rate-strengthening segments (Figure 1b). The rate-strengthening segments mimic a thin coating of viscous silicon patches (putty) placed at each end of the fault in the laboratory experiments. For simplicity, zero-displacement boundary conditions are imposed at both ends of the fault; other types of lateral boundary conditions are examined in section 8.

Model parameters also replicate the experimental setup [*Latour et al.*, 2013] (Table 1). However, the characteristic slip distance D_c, the rate-and-state parameter $a - b$, and the background loading rate $\dot{\tau}$ are not well constrained in the laboratory experiments. As a consequence we vary them within a realistic range (Table 2) to find the set of parameters that best explains the characteristics of rupture nucleation observed in the laboratory experiments with different levels of imposed normal stress. Unless otherwise noted, we set $\dot{\tau} = 0.36$ MPa/s, which is compatible with the estimated loading rate of the order of 0.4 MPa/s in the laboratory experiments of *Nielsen et al.* [2010]. In a few cases, we also vary $\dot{\tau}$ since the loading applied by a manual pump was likely slightly different in each laboratory experiment. We assume a relatively small value of D_c in the range of $0.1 - 0.5$ μm, which is found by fitting the modeled nucleation to laboratory observations (Table 2). Such a small D_c is likely related to the microscopic roughness of the abraded polycarbonate interface. Note that our simulation results do not depend on the reference friction coefficient and slip rate f_0 and V_0 as long as f_0 is greater than the change in friction associated with fault slip and healing.

We select proper numerical parameters for well-resolved simulations [*Lapusta and Liu*, 2009; *Kaneko et al.*, 2011]. The spatial cell size Δx needs to be small enough to properly resolve both the process zone size during quasi-static nucleation [e.g., *Ampuero and Rubin*, 2008] and the cohesive zone size during dynamic rupture propagation [e.g., *Kaneko et al.*, 2008]. We set Δx such that there are at least 300 node points within the nucleation length, which leads to well-resolved simulations in this study. Time t is discretized into variable time steps. The minimum value of the time step Δt_{min} is related to the time $\Delta t_{cell} = \Delta x/V_s$ needed for the shear wave to propagate through one spatial cell; it is given by $\Delta x/(3V_s) = 0.03$ μs. Such a small value of Δt_{min} is needed because slip in one time step must be comparable to or smaller than the characteristic slip D_c of the friction law to resolve the state-variable evolution. The total number of time steps is ~200,000 for each simulation.

Table 1. Model Parameters Used in the Simulations Shown in Figures 2 and 5[a]

Parameter	Symbol	Value
Shear modulus	μ	0.96 GPa
Density	ρ	1200 kg/m^3
Poisson's ratio	ν	0.35
Compressional wave speed	V_p	1860 m/s
Shear wave speed	V_s	893 m/s
Reference friction coefficient	f_0	0.60
Reference slip rate	V_0	1.0 μm/s
Characteristic slip distance	D_c	0.2 μm
Effective normal stress, $\sigma - p$	$\bar{\sigma}$	0.56–3.0 MPa
The size of the domain	L	30 cm
The size of the RW patch	L_{RW}	14 cm
Rate-and-state parameter a in RW	a	0.0100
Rate-and-state parameter a in RS	a	0.0100
Rate-and-state parameter b in RW	b	0.0144
Rate-and-state parameter b in RS	b	0.0090
Background loading rate	$\dot{\tau}$	0.24 or 0.36 MPa/s

[a]RW and RS denote rate-weakening and rate-strengthening fault patches, respectively.

In the rate-and-state framework, rock friction exhibits either rate-weakening ($a - b < 0$) or rate-strengthening ($a - b > 0$) behavior at the steady state, depending on a number of factors including normal stress, temperature, and the type of rock materials [*Marone*, 1998; *Ikari et al.*, 2011]. Models predict that rate-strengthening fault patches slip continuously and remain stable under slow tectonic loading, whereas rate-weakening fault regions can produce stick-slip motion. Under slow tectonic loading, a stick-slip frictional instability (i.e., transient slip events) can develop only if the rate-weakening region of the fault exceeds the nucleation length h^* [e.g., *Rubin*, 2008]. A theoretical estimate of h^* appropriate for the friction laws (equation (1)) was derived from the linear stability analysis of steady sliding [*Rice*, 1993; *Ruina*, 1983]:

$$h_{RR}^* = \frac{\pi}{4} \frac{\mu' D_c}{(\sigma - p)(b - a)} ,$$ (2)

where $\mu' = \mu$ for antiplane sliding and $\mu' = \mu/(1 - \nu)$ for in-plane sliding, where μ is the shear modulus and ν is the Poisson's ratio. Note that on the basis of energy balance for a quasi-statically expanding crack, *Rubin and Ampuero* [2005] derived a solution for the critical length h^* for the so-called aging law. The derivation of h^* for the slip law (equation (1)) using the same approach turned out to be more challenging because aseismic slip during the nucleation is characterized by a pulse-like behavior, with its pulse size introducing an additional unknown [*Ampuero and Rubin*, 2008].

4. Nucleation of Laboratory Earthquakes Reproduced by Numerical Simulations

Our model shows complex spatial and temporal evolution of slip on the fault. Figure 2a shows one of the simulation examples in which a sequence of characteristic shear slip events is spontaneously nucleated.

Table 2. A Range of Model Parameters Explored in this Study[a]

Parameter	Symbol	Value
Characteristic slip distance	D_c	0.1–0.5 μm
Effective normal stress, $\sigma - p$	$\bar{\sigma}$	0.56–3.0 MPa
Rate-and-state parameter b in RW	b	0.0117–0.0188
Rate-and-state parameter b in RS	b	0.0010–0.0101
Loading rate	$\dot{\tau}$	1 MPa/d–0.4 MPa/s

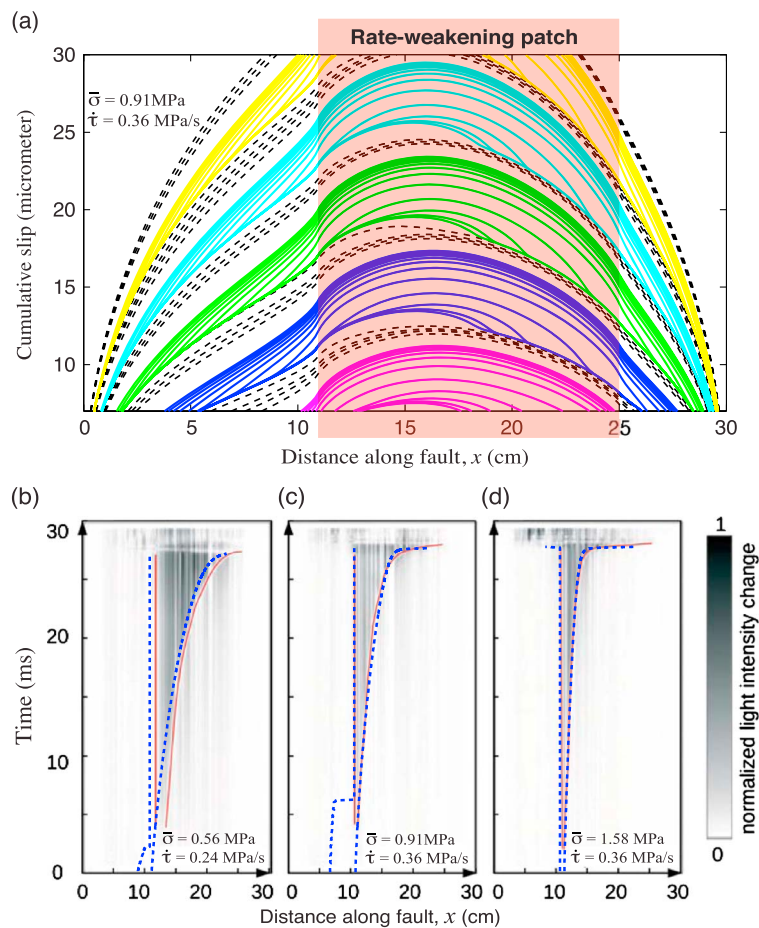[a]RW and RS denote rate-weakening and rate-strengthening fault patches, respectively.

Figure 2. Examples of spontaneous rupture nucleation in fault-slip simulations. (a) A sequence of characteristic shear slip events similar to that in the laboratory experiments [*Latour et al.*, 2013]. Cumulative slip distribution along the fault is shown. Fast shear slip events are shown by the solid lines, which are plotted with a time step of 50 μs. Dashed lines represent slower slip accumulation every 20 ms. Rate-weakening fault patch mostly experiences stick slip. (b–d) Positions of rupture fronts during a transition from quasi-static to dynamic rupture in numerical simulations with different normal stresses (blue dashed lines), which are superimposed on the positions of observed rupture tips in laboratory experiments [*Latour et al.*, 2013] (red), with a grey scale showing the light intensity change indicating the actively slipping zone. The rupture fronts are defined as the locations of two peak shear stresses: one within the left rate-strengthening patch and the other within the rate-weakening patch.

The black dashed lines show the continuous slow sliding of the rate-strengthening segments, which creates stress concentration at its tip and penetrates into the rate-weakening segment. In due time, rapid earthquake-like rupture nucleates and propagates bilaterally; its progression is shown by solid colored lines (Figure 2a). After the rapid slip event, the rate-strengthening segments experience postseismic sliding due to the transferred stress. The interevent period between two successive events is 80 ms. For each case, we select the nucleation process of the fourth event as the representative one; choosing the fifth event or sixth event leads to the same nucleation process.

Figure 3 shows the evolution of slip, slip rate, and shear stress within the rate-weakening patch during the representative nucleation process. In this relatively simple model, the peak slip rate monotonically increases during the nucleation (Figure 3b). Slip rates on a quasi-stationary portion of the fault always remain nonzero as this is a generic feature of a rate-and-state fault behavior. Such small slip rates ($< 10^{-4}$ m/s) were not resolved in the laboratory experiments. The location of the peak shear stress within the rate-weakening patch moves inward, and its propagation speed also increases monotonically (Figure 3c). The initial quasi-static rupture is unidirectional (Figure 3b). As the slip accelerates, the inertial effects become important eventually, and the rupture front propagates bilaterally during the rapid shear slip event (Figure 3b). Due to interactions with the nearby creeping region, such nucleation proceeds under temporally and spatially nonuniform stress field.
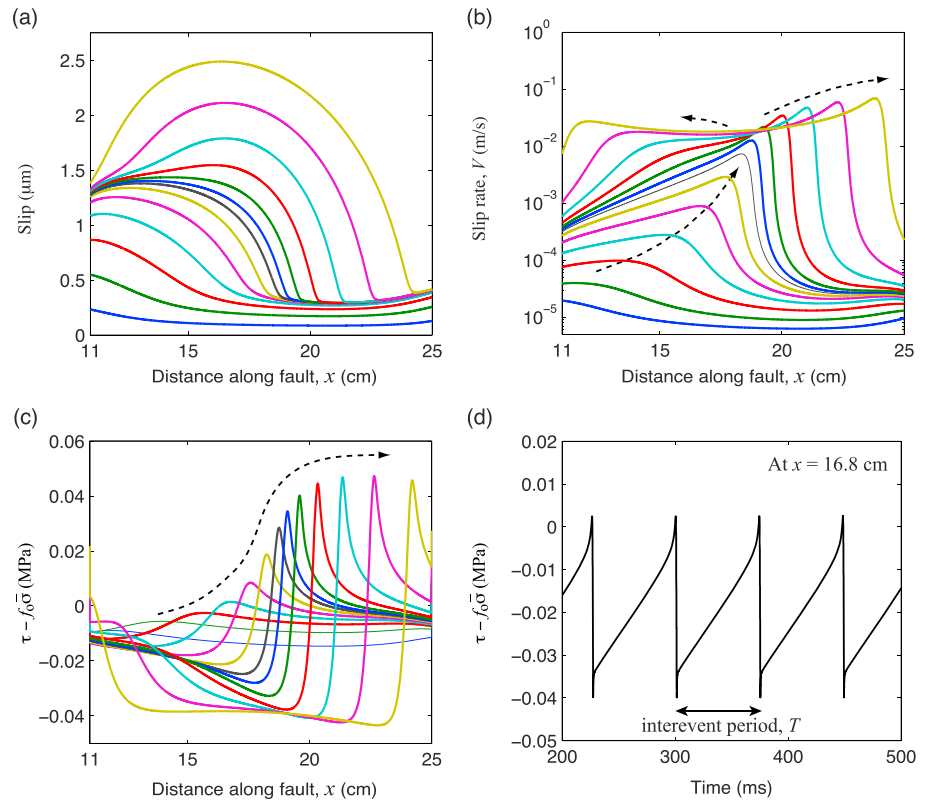
Figure 3. Snapshots of (a) slip accumulation, (b) slip rates, and (c) shear stress τ with respect to a reference stress value $f_o\bar{\sigma}$ during the nucleation process of shear slip events shown in Figure 2a. Arrows indicate the propagation direction of the peak values in each plot. (d) Shear stress versus time at $x = 16.8$ cm where the rupture length is equal to h^*_{RR} in this case.

The model described above reproduces the characteristics of shear rupture nucleation observed in the laboratory experiments of *Latour et al.* [2013]. The evolution of simulated rupture fronts fits well with that in the laboratory experiment (Figure 2d). In the modeled sequence of shear slip events, all the ruptures nucleate in the rate-weakening patch, near one of the frictional stability transitions, and propagate in the same direction (Figure 2a). This asymmetry of the rupture behavior is produced by the different sizes of the surrounding rate-strengthening patches as well as the nature of an asymmetrical nucleation process under the assumed friction laws [*Ampuero and Rubin*, 2008].

In addition, the time and length scales associated with the rupture nucleation decrease with an increasing normal stress $\bar{\sigma}$ (Figures 2b–2d). Most strikingly, the positions of the modeled and observed rupture fronts under different $\bar{\sigma}$ are in excellent agreement (Figures 2c and 2d) apart from a slight mismatch for the case with $\bar{\sigma} = 0.56$ MPa (Figure 2b) caused by a change in the location of the nucleating rupture in this laboratory experiment. However, the positions of the observed and modeled rupture fronts match if the positions of the modeled rupture fronts are shifted uniformly (Figure 4a), suggesting that in this particular experimental run, inhomogeneities introduced between runs caused the rupture to nucleate at a slightly different location.

Moreover, the evolution of the rupture front under a wide range of applied normal stress $\bar{\sigma}$ closely matches the laboratory results (Figures 5a and 5b). Three distinct phases of rupture evolution are observed regardless of $\bar{\sigma}$: quasi-static propagation characterized by the first low slope, the acceleration phase (high slope), and dynamic rupture propagation with its speed comparable to the shear wave speed of the polycarbonate (Figures 5a and 5b). During the dynamic propagation phase, the rupture is still accelerating (i.e., V_r is increasing; Figure 5a). The distance at which the rupture transitions from the quasi-static to the acceleration phase coincides with the theoretical estimate of nucleation length h^*_{RR} (Figure 5a). For example, in the simulation with $\bar{\sigma} = 0.91$ MPa (Figure 2c), $h^*_{RR} = 58$ mm, consistent with a distance at which the modeled rupture transitions from the quasi-static to the accelerating phase. A larger normal stress produces a smaller nucleation length, as expected from h^*_{RR} (open circles in Figures 5a). For $\bar{\sigma} < 0.5$ MPa, unstable slip events cannot nucleate
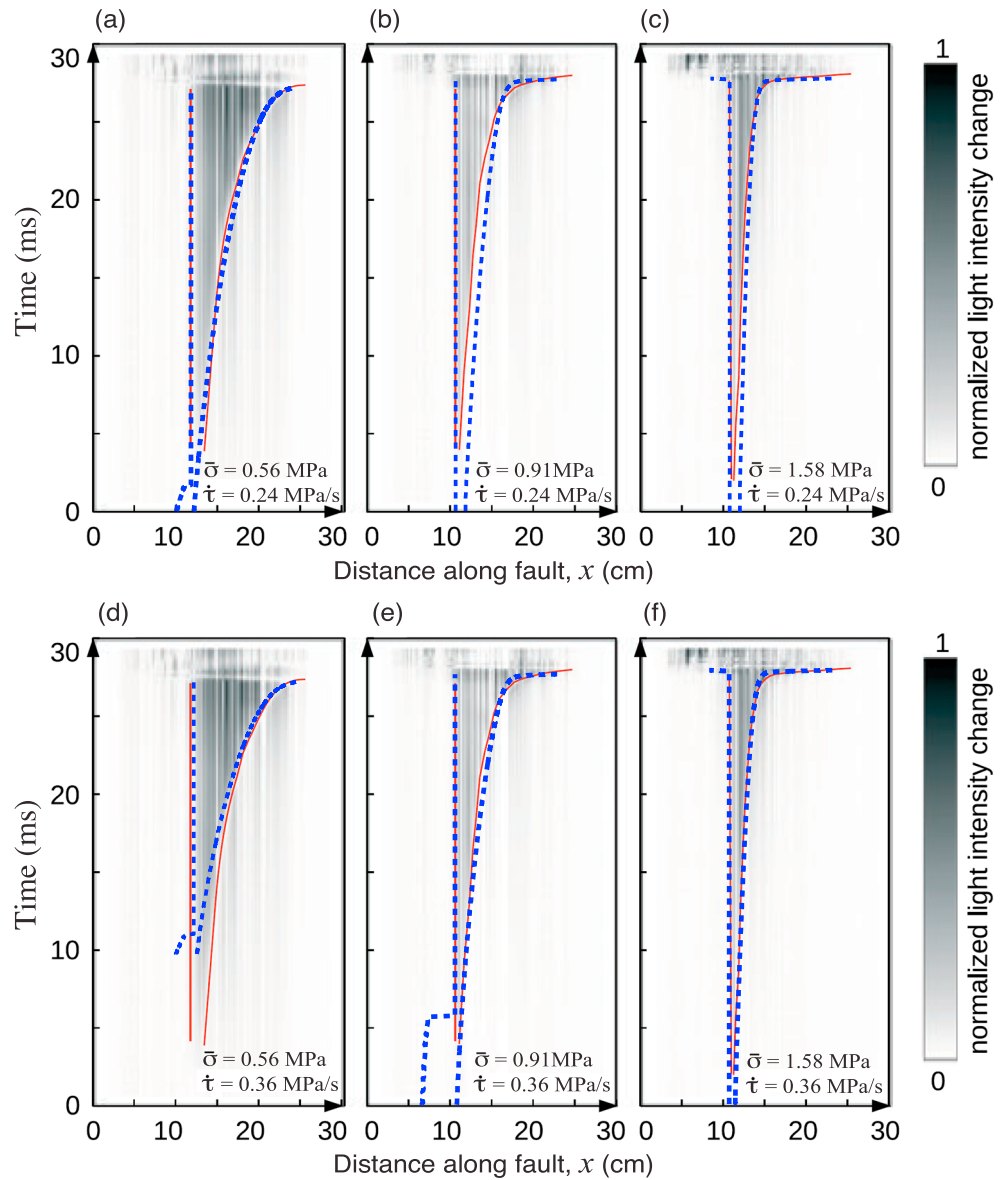
Figure 4. Dependence of simulated nucleation process on effective normal stress $\bar{\sigma}$ and background loading rate $\dot{\tau}$. (a–f) Positions of rupture fronts as a function of time during a transition from quasi-static to dynamic rupture in numerical simulations with different normal stresses and/or background loading rates. The cases shown in Figures 4a, 4e, and 4f correspond to in Figures 2b–2d, respectively. The positions of the rupture fronts in Figures 4a and 4d are slightly shifted horizontally to align with the laboratory observations [*Latour et al.*, 2013]. Assumed normal stress and background loading rate are indicated.

since h_{RR}^* becomes comparable to and greater than the size of the rate-weakening patch, consistent with the laboratory observations.

Furthermore, the peak slip rate of nucleating rupture in these simulations increases with normal stress and agrees well with those reported in these laboratory experiments (Figure 6). In the laboratory experiments of *Latour et al.* [2013], the peak slip rate was estimated from the peak velocity recorded by an accelerometer placed at $x = 19$ cm and close to the fault. We report the peak slip rate on the fault at $x = 19$ cm and compare it with that of these laboratory observations with different $\bar{\sigma}$. There is a good agreement between the simulated (red) and measured (black) peak slip rates (root-mean-square error of 5%, Figure 6c). The models (red) slightly overpredict the peak slip rates because the accelerometer was not located exactly on the fault in the laboratory experiments.
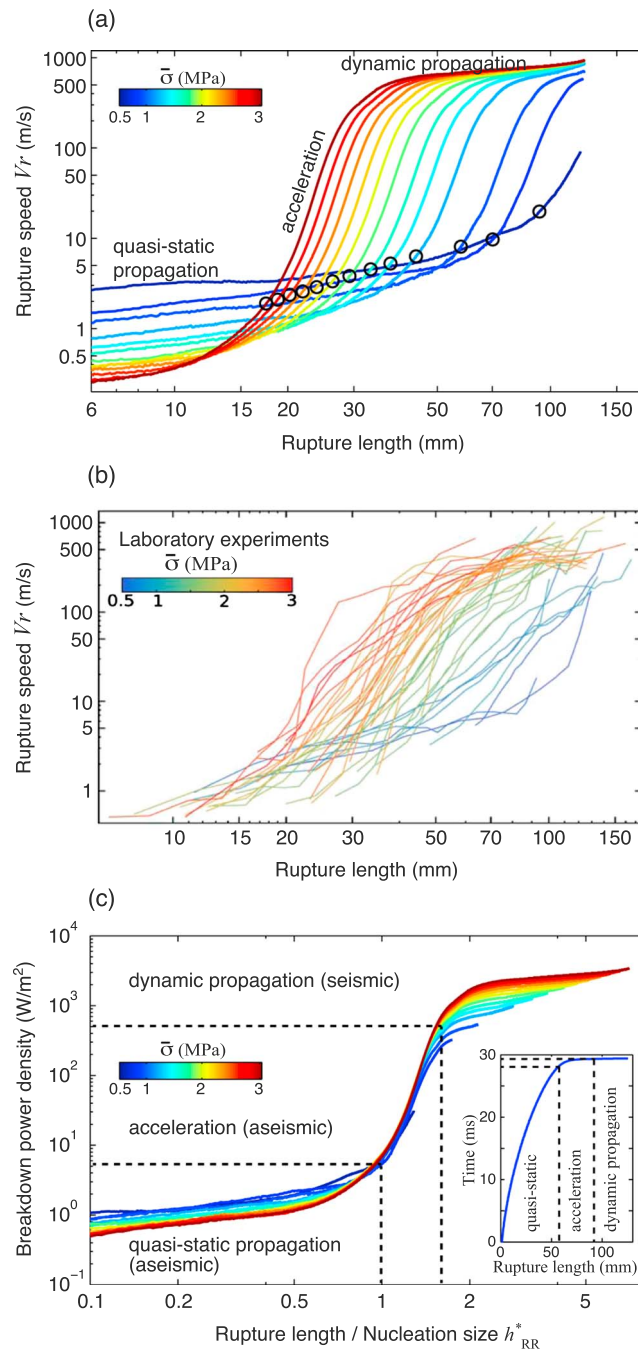
Figure 5. Characteristics of nucleation phase with different normal stresses $\bar{\sigma}$ (a) in numerical simulations and (b) for 47 stick-slip events in laboratory experiments [*Latour et al.*, 2013]. The rupture length (horizontal axis) is defined as a distance from the left edge of the rate-weakening patch to the rupture front. For all the simulations, the background loading rate is fixed at $\dot{\tau} = 0.36$ MPa/s. Rupture speed is determined by dividing the fault into intervals of 50 grid points, computing average rupture speed over each interval, and plotting the obtained value with respect to the middle of the interval. Open circles correspond to theoretical estimates of nucleation length h_{RR}^*. Observed and modeled rupture speeds increase with the rupture length. (c) The curves obtained from the numerical simulations are collapsed after renormalizing the horizontal axis with h_{RR}^* and plotting the breakdown power density $(\pi/2)(\Delta\tau^2/\mu')V_r$ instead of V_r. The inset shows the rupture evolution for the case with $\bar{\sigma} = 0.91$ MPa.
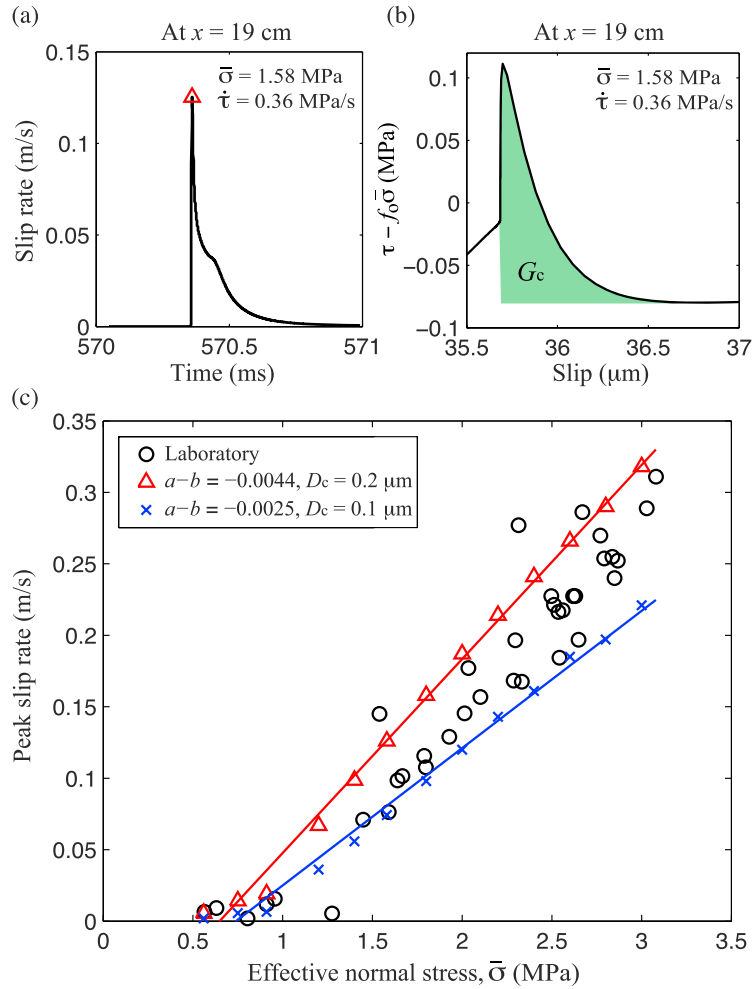
Figure 6. (a) Slip rate and (b) shear stress, $\tau - f_0 \bar{\sigma}$, at $x = 19$ cm on the fault during a representative event for $\bar{\sigma} = 1.58$ MPa shown in Figure 2d. The triangle corresponds to the peak slip rate. The green area under the slip-weakening curve shows the effective fracture energy G_c. (c) Peak slip rate during a shear slip event for different $\bar{\sigma}$ in the laboratory experiments (black circles), the models shown in Figure 5a (red triangles), and another set of models shown in Figure 8c (blue crosses). The lines are the least squares fits to the model results. The root-mean-square (RMS) error between the data (black) and model (red) is 0.042 m/s, and the RMS percentage error is 5.0%.

A notable aspect not reported in the laboratory study of *Latour et al.* [2013] is that the timescale of nucleation also depends on background loading rate $\dot{\tau}$. For a given normal stress $\bar{\sigma}$, the timescale of simulated nucleation decreases with increasing $\dot{\tau}$ (Figure 4). Slight disagreements between observed and simulated rupture evolution with a range of normal stresses shown in Figures 5a and 5b are likely caused by differences in the loading rates. In each laboratory experiment shown in Figures 5b, the background loading rate was perhaps slightly different, whereas the same loading rate is assumed in these simulations. The dependence of rupture propagation speeds on background loading is further discussed in section 7.

5. The Scaling of Rupture Nucleation Behavior

We find that the behavior of nucleating ruptures can be rescaled based on a general energy balance argument. The total elastic energy released by a quasi-static crack of the length ℓ in a slab of the thickness w is $U = (1/4)(\Delta\tau^2/\mu')\pi\,\ell^2 w$, where $\Delta\tau$ is the stress drop (which is uniform within the ruptured region) [*Lawn*, 1993]. The energy flow per unit crack advancement per unit slab thickness (i.e., $w = 1$) in the direction of ℓ can be obtained by taking a derivative with respect to ℓ: $G = \partial_\ell U = (\pi/2)(\Delta\tau^2/\mu')\ell$. For an advancing crack with the propagation speed V_r, the energy release rate per unit time per unit area can be expressed as

$$\frac{dG}{dt} = \frac{dG}{d\ell}\frac{d\ell}{dt} = \frac{\pi}{2}\frac{\Delta\tau^2}{\mu'}V_r = \frac{GV_r}{\ell}, \qquad (3)$$

which we refer to as "breakdown power density." The Griffith energy balance requires that the fracture energy G_c dissipated at the crack tip per unit front advancement (Figure 6b) is equal to the elastic energy release rate G. Note that G in equation (3) is often called the static energy release rate per unit crack length. Dynamic energy release rate, which can account for elastodynamic effects, is the product of G and a universal function that depends on the rupture speed [e.g., *Freund*, 1998].

Figure 5c shows that by scaling the rupture speed V_r by G/ℓ and renormalising the rupture length with h_{RR}^*, the individual curves collapse in a consistent way. Stress drop $\Delta\tau$ in evaluating the breakdown power density is obtained by $\Delta\tau = T\dot{\tau}$, where T is the interevent period and $\dot{\tau}$ is the background stressing rate (Figure 3d). Since breakdown power density is proportional to V_r, each curve maintains the same shape as in Figure 5a. The collapse of the curves occurs because the rupture speed in the quasi-static propagation phase for a larger $\bar{\sigma}$ is smaller, but the corresponding stress drop $\Delta\tau$ is larger. Consequently, three distinct phases of nucleation can be clearly identified for all the cases with different $\bar{\sigma}$: quasi-static propagation, acceleration phase, and dynamic rupture propagation (Figure 5c). The breakdown power density in the dynamic propagation phase varies by an order of magnitude likely because equation (3) does not account for the dynamic energy release rate as well as other complexities arising from in-plane dynamic rupture propagation. For all the nucleating ruptures shown in Figure 5a, a critical breakdown power that signifies the transition from the quasi-static to the acceleration phase is 5.6 W m^{-2}. This means that the product $\Delta\tau^2 V_r$ in equation (3) must exceed a critical value for the rupture speed to increase rapidly. Our results suggest that breakdown power density and critical nucleation length control the scaling of rupture nucleation behavior under a wide range of normal stress conditions.

To see whether the inertial (wave) effect plays a role during the acceleration phase, we perform additional quasi-static simulations (Figure 7). The result shown in Figure 7b is obtained by first simulating earthquake cycles up to the end of the third seismic event and then continuing with a quasi-static simulation (by turning off the inertial effects) until the numerical solution ceased to exist due to high acceleration at the onset of the subsequent event. Despite the quasi-static assumption, the acceleration phase still appears in this case and is almost identical to that in the fully dynamic case (Figures 7a and 7b). This means that the inertial effect on the growth of nucleating rupture is negligible during the acceleration phase, indicating that this phase is an aseismic process.

At the end of the acceleration phase, the rupture speeds are about 22 to 35% of the shear wave speed (Figure 7c). Because the determination of rupture speeds requires spatial averaging, the actual rupture speeds at the end of the quasi-static simulations shown in Figure 7c are somewhat underestimated. These results suggest that rupture speeds can reach tens of percent of the shear wave speed of the medium during the acceleration phase even though the inertial effect on the growth of rupture is negligible in this phase.

6. Rate-and-State Constitutive Parameters Inferred From Simulations

From our simulations and laboratory observations, the rate-and-state parameter $b - a$ and characteristic slip distance D_c of the polycarbonate interface can be inferred, although $b - a$ and D_c are not uniquely determinable. Different combinations of $b - a$ and D_c in the rate-weakening patch can also explain a set of laboratory observations equally well (Figure 8). For example, reducing both D_c and $b - a$ by a factor of 2 leads to similar rupture evolution as shown in the previous set of simulations (compare Figures 8c and 5a). Since modeled nucleation length h^* is approximately proportional to $D_c/(b - a)$ (as shown in equation (2)), the same h^* can be obtained for many combinations of D_c and $b - a$. Yet the actual values of $b - a$ and D_c for the polycarbonate interface cannot vary more than a factor of ~2 from the inferred values to be consistent with observed peak slip rates that also depend on $b - a$ (Figure 6c). Despite the nonuniqueness, the general characteristics of the modeled nucleation processes under a range of $\bar{\sigma}$ remain unchanged (Figure 8d).

The experimental conditions would be better constrained if rate-and-state parameters (a, b, and D_c) of the polycarbonate could be measured using velocity-step laboratory experiments [e.g., *Marone*, 1998]. However performing velocity-step experiments of a plastic material such as polycarbonate is challenging. With the current experimental procedures, we find that the relatively low stiffness of the material systematically results in stick-slip behavior, preventing an accurate measurement of direct and evolution effects (not shown here). Future developments of experimental techniques may allow to improve such measurements.
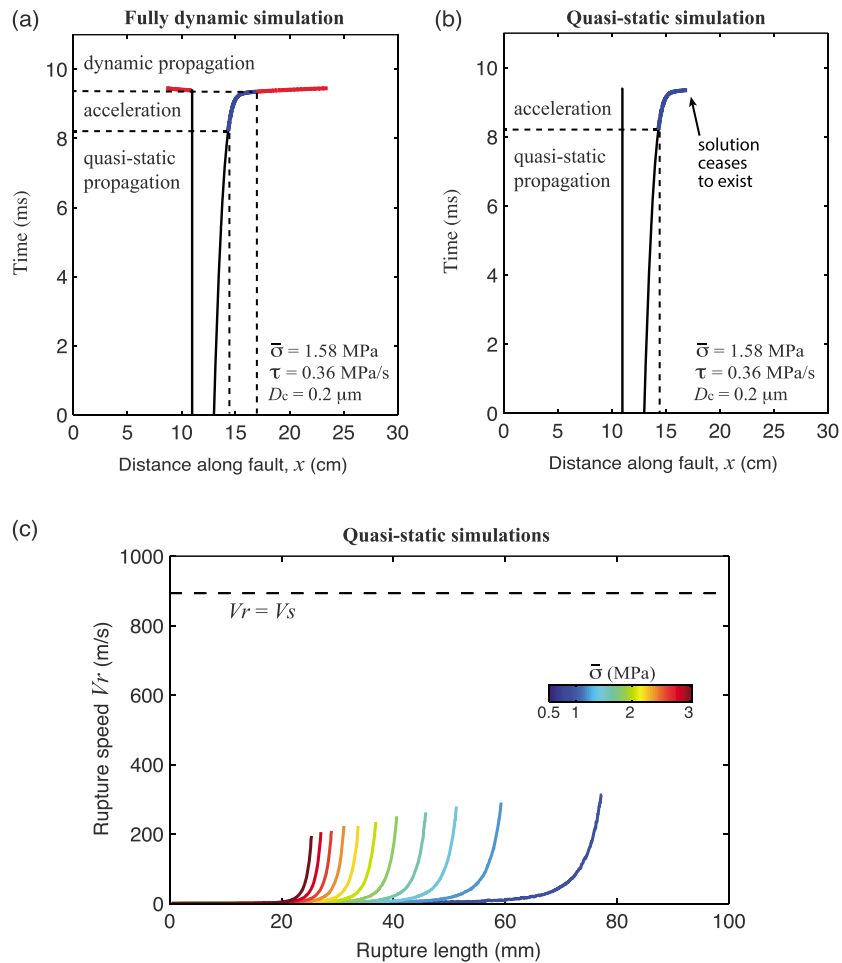
Figure 7. Examples of a nucleation process in (a) fully dynamic simulation and (b) quasi-static simulation. The nucleation process in the quasi-static case is obtained by first simulating three earthquake cycles with the inertial effects then continuing with a quasi-static simulation by turning off the inertial effects. The acceleration phase (blue) occurs despite the quasi-static assumption, indicating that the acceleration phase is still a quasi-static (aseismic) process. (c) Rupture speeds in quasi-static simulations with different normal stresses $\bar{\sigma}$. The corresponding fully dynamic cases are shown in Figure 5a. At the end of each curve, the solution ceases to exit.

7. Influence of Different Background Loading Rates and Loading Conditions on the Propagation Speed of Quasi-Static Rupture

To understand the robustness of our results, we further consider scenarios with different loading rates and conditions. Decreasing background loading $\dot{\tau}$ from a laboratory to tectonic deformation rate results in a slower propagation speed during the quasi-static phase (Figure 9). Rupture propagation speeds during the quasi-static phase approximately scale with the background loading rate (Figure 9). Slower loading also leads to up to a factor of 2.5 larger nucleation length (Figure 9). These results are qualitatively consistent with earlier laboratory observations [*Kato et al.*, 1992; *Ohnaka*, 1996] and numerical results [*Kato and Hirasawa*, 1996; *Kaneko and Lapusta*, 2008]. In addition, a set of simulations with a slower loading condition show that critical breakdown power at the transition from the quasi-static to the acceleration phase decreases with the background loading rate (compare Figures 5c and 10). Since critical breakdown power depends on the background loading rate, it is not a material or interface property. Furthermore, replacing the rate-strengthening segments in the model with slightly rate-weakening regions leads to different characteristics of rupture nucleation (Figure 11). The change in friction properties in the vicinity of the nucleation zone directly affects the loading conditions and the energetics of the crack tip propagation. The fact that a wide range of propagation speeds (10^{-5} - 10^3 ms^{-1}) can be observed by fine tuning the background loading rate (Figure 9) highlights
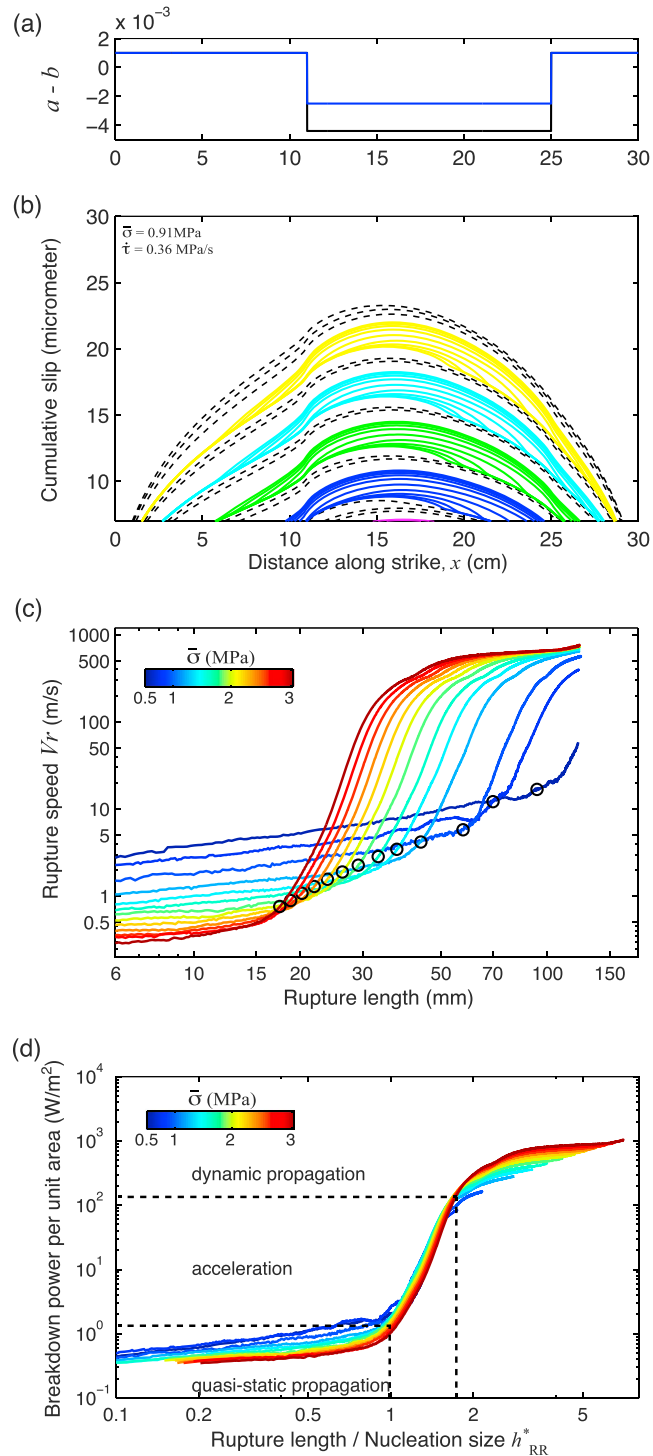
Figure 8. Examples of spontaneous rupture nucleation in fault-slip simulations with $a - b = -0.0025$ and $D_c = 0.1$ μm in the rate-weakening patch. (a) Distribution of friction parameter $a - b$ in this case (blue) and that used in Figure 5a (black). (b) Cumulative slip distribution along the fault is shown. Fast shear slip events are shown by the solid lines, which are plotted with a time step of 50 μs. Dashed lines represent slower slip accumulation every 20 ms. (c) Characteristics of nucleation phase under different normal stresses $\bar{\sigma}$. The background loading rate is fixed at $\dot{\tau} = 0.36$ MPa/s in these simulations. Open circles correspond to theoretical estimates of nucleation length h_{RR}^*. (d) The curves obtained from the numerical simulations are collapsed after renormalizing the horizontal axis with h_{RR}^* and plotting the breakdown power per unit area $(\pi/2)(\Delta\tau^2/\mu')V_r$ instead of V_r.
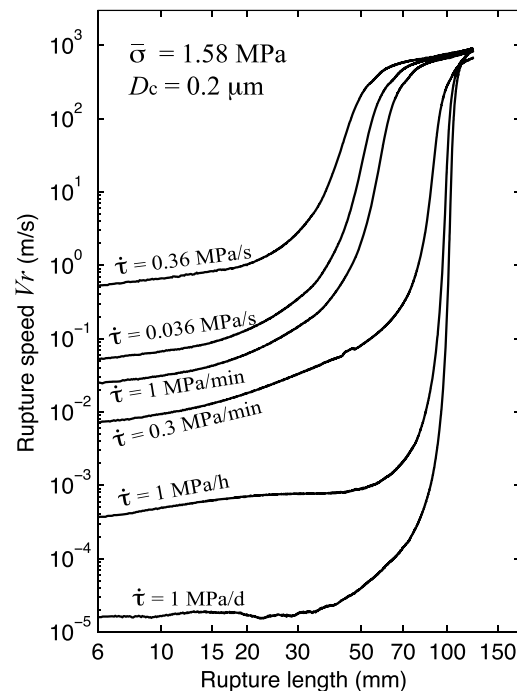
Figure 9. Characteristics of nucleation phase under different background loading rates $\dot{\tau}$ for polycarbonate block with $\bar{\sigma} = 1.58$ MPa. Decreasing the background loading rate $\dot{\tau}$ leads to a larger nucleation length.

the importance of loading conditions in interpreting laboratory observations. The wide variety of slow rupture behaviors for a nominally flat frictional interface observed in previous laboratory studies [*Ben-David et al.*, 2010; *Nielsen et al.*, 2010; *Latour et al.*, 2013; *Svetlizky and Fineberg*, 2014] could have resulted from different loading rates or configurations.

8. Discussion

8.1. On Different Slip-Boundary Conditions at the Fault Edges
As described in section 3, we have assumed zero-displacement boundary conditions at the edges of the fault for simplicity. However, the lateral boundary conditions in these laboratory experiments are close to free slip. The numerical methodology we have employed cannot accurately represent free slip-boundary conditions in this particular configuration. To see the potential effect of free-slip boundaries on the resulting rupture growth, we have replaced the zero-displacement boundaries with the constant-velocity boundaries and conducted a set of simulations using the same model parameters as those in Figure 5a. Figure 12b shows that the resulting slip accumulation patterns within the rate-weakening patch remain similar to those shown in Figure 2a, while additional slow slip (indicated by a black arrow) emerges due to a stress concentration near the right frictional transition at $x = 25$ cm. This stress concentration is produced by additional loading associated with the velocity boundaries, especially since the boundary at $x = 30$ cm is close to the frictional transition located at $x = 25$ cm (Figure 12b). As a result, the behavior of rupture nucleation with smaller $\bar{\sigma}$ that leads to a larger nucleation length is complicated by the stress concentration (Figures 12c and 12d). In one of these cases, the speed of dynamic rupture exceeds the shear wave speed of the medium (Figures 12c) because of the stress concentration, the phenomena studied by *Liu and Lapusta* [2008]. On the other hand, the general characteristics of the nucleation processes under a range of $\bar{\sigma}$ remain unchanged (Figures 12c and 12d), implying that the lateral boundary conditions do not affect our main conclusions.

8.2. On Different Loading Conditions Between Laboratory Experiments and Numerical Models
In our models, we have assumed only shear background loading $\dot{\tau}$, whereas in the laboratory experiments of *Latour et al.* [2013], the vertical load on an inclined fault generates normal stress loading $\dot{\sigma}$ proportional to shear stress loading (Figure 1a). The fault geometry in *Latour et al.* [2013] suggests that $\dot{\sigma}$ is 2.6 times larger than $\dot{\tau}$. While the numerical scheme used in this study cannot handle such large $\dot{\sigma}$ currently, we consider additional nucleation scenarios with both shear stress loading and normal stress loading (Figure 13). Including normal
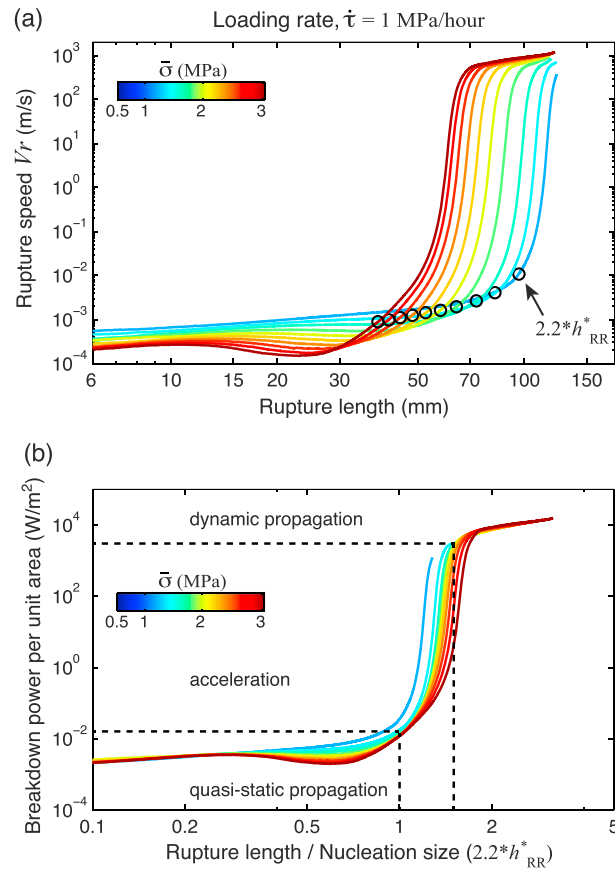
Figure 10. (a) Characteristics of nucleation phase with a slower loading rate. For all the simulations, the background loading rate is fixed at $\dot{\tau}$ = 1 MPa/h, which is about 1000 times slower than that of the laboratory experiments. Open circles correspond to nucleation lengths $2.2h_{RR}^*$, each of which is obtained from the intersection of the first low slope and the second high slope. (b) The curves obtained from the numerical simulations are collapsed after renormalizing the horizontal axis with $2.2h_{RR}^*$ and plotting the breakdown power per unit area $(\pi/2)(\Delta\tau^2/\mu')V_r$ instead of V_r.

stress loading in our model leads to a sequence of noncharacteristic slip events, with each nucleation episode being different from the previous one due to evolving normal stresses (Figure 13b). We find that the timescale of nucleation processes is affected by the normal stress loading because of more complex evolution of slip during the sequence. Nevertheless, the general characteristics of the nucleation remain the same as those without normal stress loading (Figures 13c and 13d). While our results suggest that accounting for normal stress loading does not seem essential for capturing the first-order experimental observations, future work is needed to accurately represent the actual loading condition.

8.3. Comparison of a Critical Nucleation Length in Simulations to a Theoretical Estimate

In many scenarios considered in this study, which include cases with different a/b in the rate-weakening patch, the rupture length at the transition from the quasi-static to the acceleration phase is consistent with a theoretical estimate given by h_{RR}^* (equation (2)) (e.g., Figures 5 and 8). In contrast, when the background loading rate is slower than the typical laboratory rate, the transition length becomes up to a factor of 2.5 larger than h_{RR}^* (Figures 9 and 10). Future work may be directed toward theoretical analysis of a critical nucleation length accounting for the background loading rate.

8.4. Parameters Controlling the Scaling of Laboratory Results

We have shown that by scaling rupture speed V_r with G/ℓ and renormalising the rupture length with theoretical estimate of a nucleation length h_{RR}^*, the individual curves collapse in a consistent way (e.g., Figure 5c). This scaling works quite well even though our definition of breakdown power density (equation (3)) assumes uniform stress drop. Since shear stresses are nonuniform in the actively slipping zone and are evolving with time (Figure 3c), we have estimated $\Delta\tau$ using a simple method (i.e., $\Delta\tau = T\dot{\tau}$). However, during the quasi-static
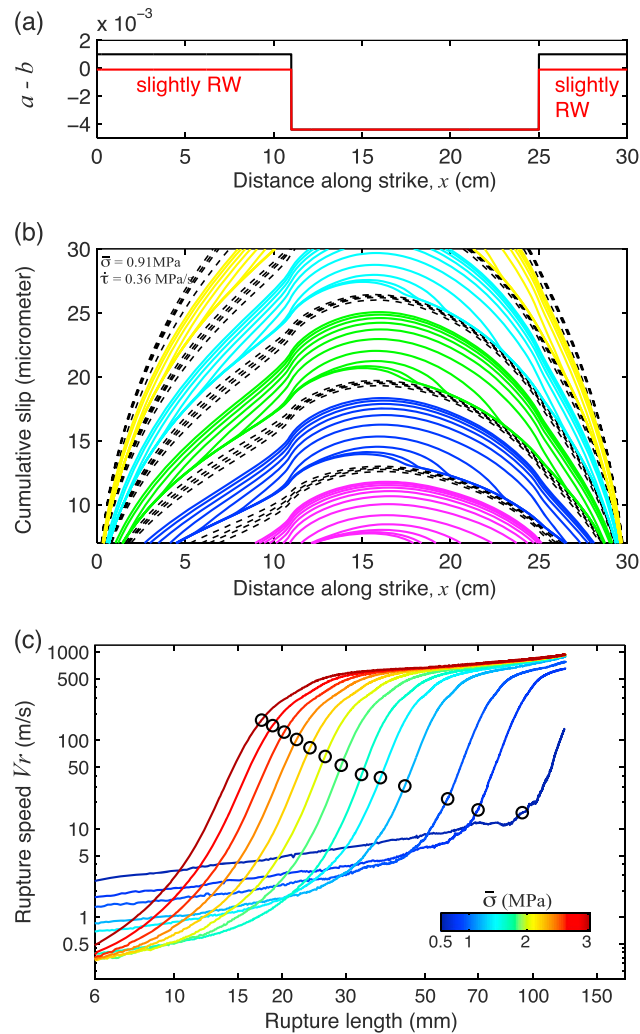
Figure 11. Examples of spontaneous rupture nucleation in fault-slip simulations with only rate-weakening fault patches. (a) Distribution of friction parameter $a - b$ in this case (red) and that used in Figure 5a (black). (b) Cumulative slip distribution along the fault is shown. Fast shear slip events are shown by the solid lines, which are plotted with a time step of 50 μs. Dashed lines represent slower slip accumulation every 20 ms. (c) Characteristics of nucleation phase under different normal stresses $\bar{\sigma}$. The loading rate is fixed at $\dot{\tau} = 0.36$ MPa/s in these simulations. Open circles correspond to theoretical estimates of nucleation length h_{RR}^*, which do not coincide with the transition from the quasi-static to the acceleration phases. The spread of the curves is larger than that of the laboratory results shown in Figure 5b.

propagation phase, the stress drops are smaller than $\Delta\tau$ estimated from the simple method (Figures 3c and 3d).

To understand how this particular way of estimating $\Delta\tau$ affects the resulting breakdown power density and scaling, we calculate $\Delta\tau$ using another approach where $\Delta\tau$ is defined as the shear stress difference between the quasi-uniform level ahead of rupture front and the lowest point (near the end of the process zone) at the end of the acceleration phase (Figures 14a and 14b). Although the resulting $\Delta\tau$ is systematically smaller than the previous estimates based on $\Delta\tau = T\dot{\tau}$, the collapse of curves still occurs, confirming that breakdown power density is an appropriate parameter controlling the scaling (Figure 14c).

Latour et al. [2013] argued that their experimental curves can be collapsed by using observed nucleation lengths and estimated "surfacic power" for the scaling, the latter defined as the product of the absolute level of shear stress and the peak slip rate on the fault. The fact that our modeling results are independent of reference coefficient of friction f_0 and hence of the absolute level of shear stress suggests that surfacic power does not play a role in these laboratory experiments. On the other hand, once the normal stress becomes large
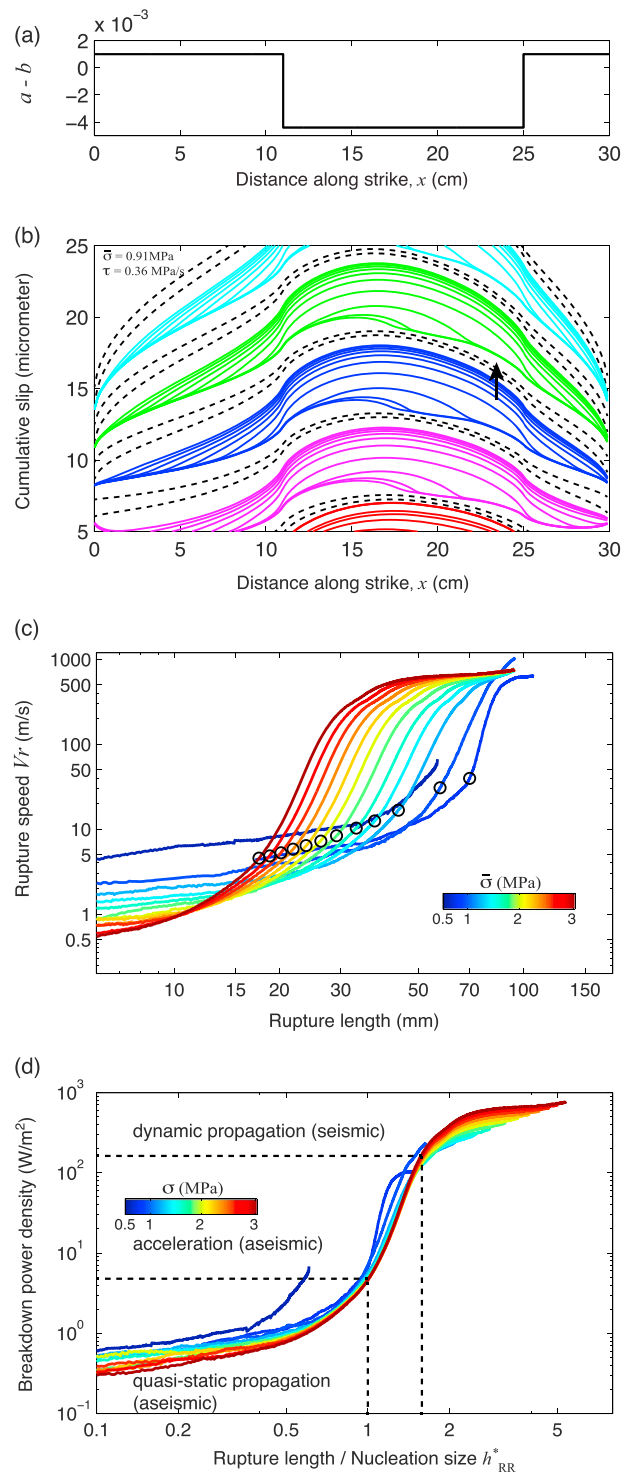
Figure 12. Examples of spontaneous rupture nucleation in fault-slip simulations where velocity boundary conditions $V_{BC} = 60$ μm/s are imposed at $x = 0$ and $x = 30$ cm. (a) Distribution of friction parameter $a - b$. (b) Cumulative slip distribution along the fault is shown. The black arrow indicates the location of slow slip, which is caused by a stress concentration resulting from additional loading associated with the velocity boundaries. (c) Characteristics of nucleation phase under different normal stresses $\bar{\sigma}$. The loading rate is fixed at $\dot{\tau} = 0.36$ MPa/s in these simulations. Open circles correspond to theoretical estimates of nucleation length h^*_{RR}. (d) The curves obtained from the numerical simulations are collapsed after renormalizing the horizontal axis with h^*_{RR} and plotting the breakdown power per unit area $(\pi/2)(\Delta\tau^2/\mu')V_r$ instead of V_r. The outlier (the case with $\bar{\sigma} = 0.56$ MPa) is affected by the stress concentration near the right RW-RS transition.
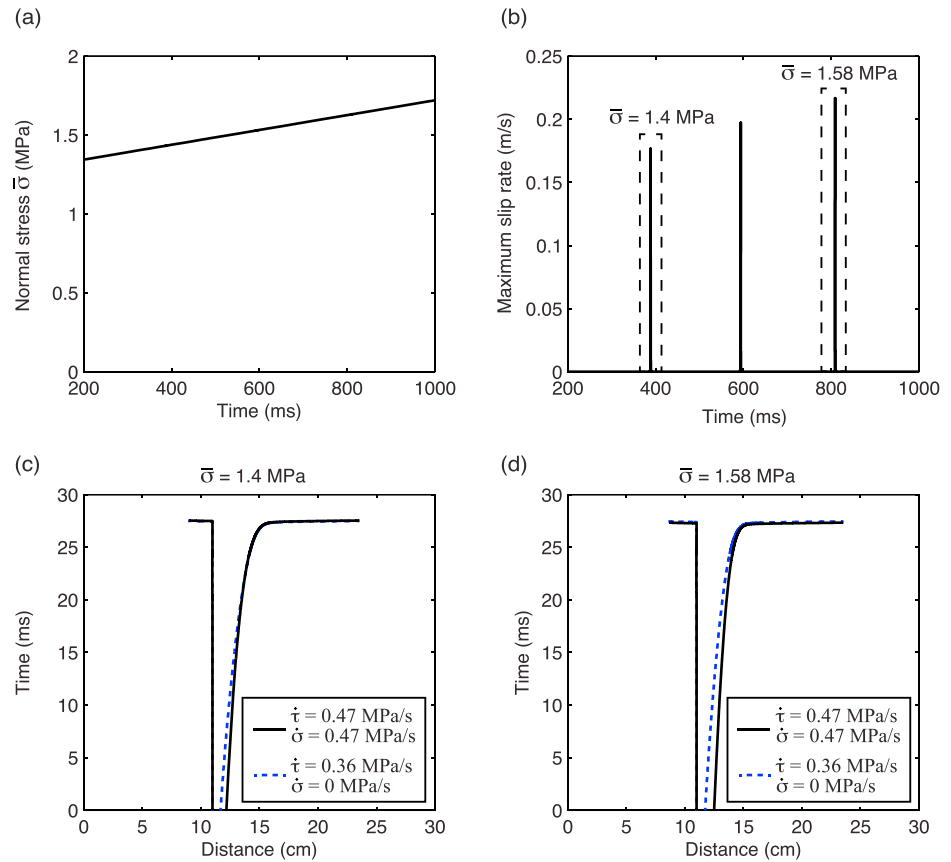
Figure 13. Simulated nucleation processes with both shear stress loading and normal stress loading. In this simulation, the normal stress loading $\dot{\sigma}$ is 0.47 MPa/s, equal to the shear stress loading $\dot{\tau}$. (a) Normal stress versus time during a sequence of shear slip events. The normal stress increases with time due to normal stress loading. (b) The maximum slip rate on the fault versus time. The maximum slip rate is larger for a latter event due to increasing normal stresses. (c) Evolution of rupture fronts during nucleation at which $\bar{\sigma}$ is approximately equal to 1.4 MPa indicated in Figure 13b. The blue dashed curve corresponds to an equivalent case without normal stress loading shown in Figure 5a. (d) The same as Figure 13c except for $\bar{\sigma} = 1.58$ MPa. Normal stress loading affects the timescale of the nucleation.

enough such that shear heating becomes important [e.g., *Di Toro et al.*, 2011], surfacic power may become a key parameter controlling the scaling. Nevertheless, both our analysis and that of *Latour et al.* [2013] suggest that elastic power and critical nucleation length control the scaling of the nucleation of shear ruptures in these experiments.

From the scaling of nucleating ruptures, we have identified three rupture propagation phases: the initial quasi-static propagation phase and the faster acceleration phase followed by dynamic rupture propagation that radiates seismic waves. Our results suggest that the transition from the quasi-static to the acceleration phase can be understood from the stability of a rate-and-state fault or critical nucleation length. In contrast, the transition from the acceleration to the dynamic propagation phase is determined by the degree of inertial effect. Compared to the stable growth of rupture in the quasi-static propagation phase, unstable growth of rupture in the acceleration phase is characterized by much larger breakdown power density (e.g., Figure 5c). Our result is also consistent with previous numerical studies [e.g., *Rubin*, 2008; *Wei et al.*, 2013] in that fault segments slightly larger than the critical nucleation length only generate episodic slow slip events, as the rupture in these segments can only reach the acceleration phase (i.e., no dynamic propagation).

The concept of breakdown power is closely related to that of fracture energy but includes an idea about how fast the elastic energy is transferred to the rupture tip. For a given background loading rate, the existence of a critical power at the transition from the quasi-static to the acceleration phase suggests that the product $\Delta\tau^2 V_r$ must exceed a critical value for the rupture speed to increase rapidly (section 5). At the same time, a critical breakdown power is not a material property as it depends on the loading conditions and background loading
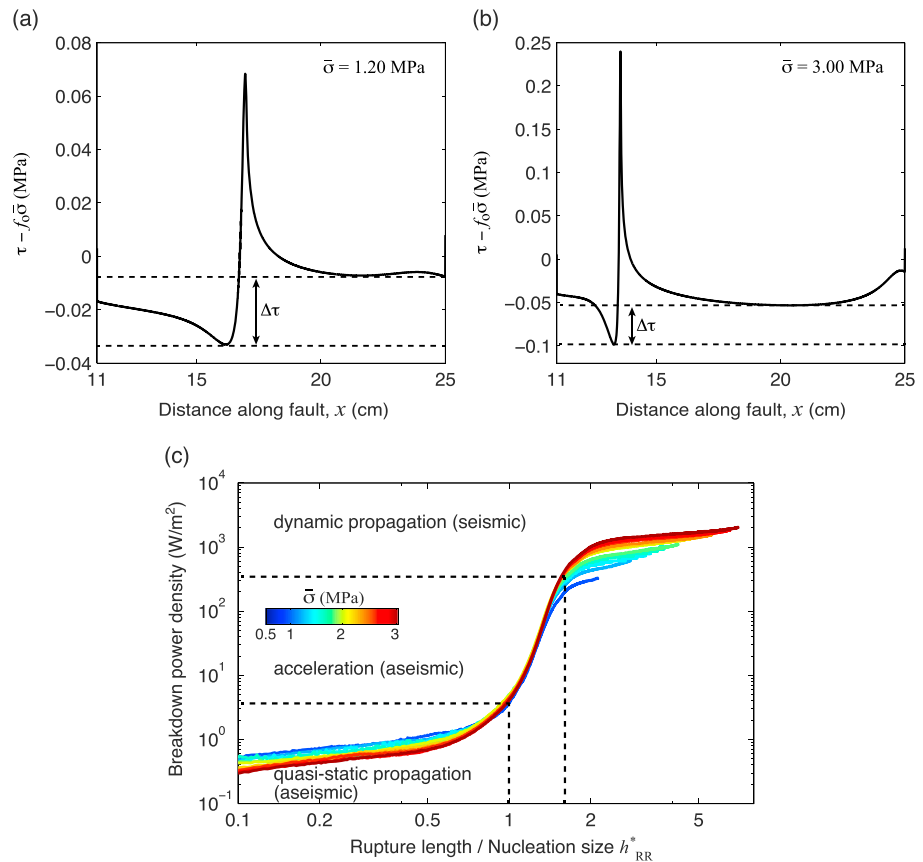
Figure 14. Shear stress distribution in the rate-weakening fault patch at the end of the acceleration phase for (a) $\bar{\sigma} = 1.2$ MPa and (b) $\bar{\sigma} = 3.0$ MPa. These cases correspond to those shown in Figure 5a. (c) The same as Figure 5c except that stress drop $\Delta\tau$ in breakdown power density (equation (3)) is estimated from the difference between the level of shear stress ahead of the rupture and the lowest point as indicated in Figures 14a and 14b. Despite the different way for estimating $\Delta\tau$, the scaling by the breakdown power density works well for the quasi-static and acceleration phases.

rate (section 7). We must conclude that the precise physical meaning of breakdown power density remains to be understood, and further work is needed to test whether the same concept applies to the nucleation of laboratory earthquakes in other studies and to other fault models.

8.5. Slip Law Versus Other State-Variable Evolution Laws

We have assumed the slip law for the evolution of state variable in the rate-and-state framework. There are several variants of state-variable evolution laws [*Dieterich*, 1978; *Ruina*, 1983; *Kato and Tullis*, 2001; *Nagata et al.*, 2012] including the most widely used "aging law." Previous studies [*Ampuero and Rubin*, 2008; *Rathbun and Marone*, 2013] showed that the slip law fits existing velocity-step laboratory data better than the aging law does and hence is more appropriate for earthquake nucleation. At the same time, existing laboratory experiments are limited to velocity jumps of about 2 orders of magnitude. Because much larger velocity increases occur at the leading edge of expanding nucleation zones (Figure 3b), it would be of interest to see if this superiority of the slip law is maintained for much larger velocity increase in these laboratory experiments. Whether numerical models with the aging law and other variants can still reproduce the same characteristics of rupture nucleation remains a question for future study.

8.6. Nucleation Processes Reported in Kaneko and Ampuero [2011] and Their Relation to This Study

Motivated by the laboratory study of *Nielsen et al.* [2010], *Kaneko and Ampuero* [2011] used a numerical model similar to that in this study and reproduced the laboratory observations of slow and steady (i.e., constant V_r) rupture fronts. Unlike this study, *Kaneko and Ampuero* [2011] considered parameters relevant to crustal conditions and focused on the mechanism of slow and steady rupture fronts, which are generated by the coalescence of inward migrating creep fronts under a limited range of conditions where the rate-weakening

patch is smaller than twice the penetration distance of an inward creep front. While the presence of slow and steady (i.e., constant V_r) rupture fronts reported in previous laboratory studies [*Ohnaka*, 1996; *Nielsen et al.*, 2010] may be due to low resolution of the laboratory data, *Kaneko and Ampuero* [2011] suggested that the propagation of such fronts can occur under some circumstances where a stress concentration (e.g., the coalescence of creep fronts) interacts with the nucleating rupture. In contrast, rupture nucleation characterized by unsteady (i.e., nonconstant V_r) rupture front (e.g., Figure 2) is not limited to a narrow range of parameters and would be applicable to a more general situation where the nucleation emerges in the vicinity of the transition from a creeping to locked segment.

8.7. Nucleation Processes Reported in Ampuero and Rubin [2008] and their Relation to This Study

Nucleation processes on a rate-and-state fault with the slip law were studied in detail by *Ampuero and Rubin* [2008]. However, we have found that creeping fault segments, which were not considered in *Ampuero and Rubin* [2008], influence the loading conditions in the nearby rate-weakening region and complicate the rupture nucleation behavior (section 7). The importance of loading conditions was also demonstrated by *Kaneko and Ampuero* [2011] where a crack-like expansion of rupture growth can occur in simulations with the slip law under some conditions as described above.

8.8. Implications for Earthquake Nucleation on Natural Faults

Since the same characteristics of rupture nucleation have been observed in both laboratory and numerical experiments, it is reasonable to assume that the same mechanism applies to at least a subset of earthquake nucleation on crustal faults. In section 4, we have shown that the distance at which the rupture transitions from the initial quasi-static phase to the acceleration phase is roughly the same as theoretical estimate h^*_{RR} (equation (2)) (although the background loading is not accounted in the derivation of the critical length further influences the transition distance). This means that the critical nucleation length of crustal earthquakes can be estimated roughly via h^*_{RR}. We assume parameters appropriate to conditions at seismogenic depths characterized by a larger shear modulus $\mu' = 30$ GPa and characteristic slip distance $D_c = 10 - 200$ μm, a typical range found in rock-friction laboratory experiments [*Ikari et al.*, 2011; *Carpenter et al.*, 2014]. If we further assume that a typical range of friction parameter $b - a = 5 \times 10^{-4} - 5 \times 10^{-3}$ and effective normal stress $\sigma - p = 10 - 100$ MPa, then $h^*_{RR} = 0.5 - 1000$ m at seismogenic depths. The estimated h^*_{RR} can further increase if the pore fluid pressure is near lithostatic such that $\sigma - p \sim 1$ MPa, the condition often assumed to explain slow slip events on subduction zones [e.g., *Liu and Rice*, 2005] and creep events on crustal faults [e.g., *Wei et al.*, 2013]. This example illustrates that the reliable extrapolation of friction parameters to values relevant for natural faults remains difficult as friction parameters $b - a$ and D_c greatly vary depending on a number of factors including normal stress, temperature, and the type of rock materials [e.g., *Marone*, 1998; *Ikari et al.*, 2011; *Carpenter et al.*, 2014] in addition to poorly constrained fluid pressure in the fault zone at seismogenic depths. Nevertheless, the upper bound of the estimated h^*_{RR} indicates that the same nucleation mechanism may apply to kilometer-wide nucleation zones inferred from foreshock observations [*Dodge et al.*, 1996; *Bouchon et al.*, 2011]. The scaling of nucleation length with h^*_{RR} further supports an existing idea that the critical nucleation length of crustal earthquakes, which may be manifested by the size of foreshock zones, would be larger in regions with higher fluid pressure or larger critical slip distance. Our results further indicate that the migration speed of foreshocks, if triggered by the quasi-static propagation of slow rupture, would be faster in the region of low effective normal stress and hence high fluid pressure in the fault zone (Figure 5a). Hence, analysis of spatially evolving foreshocks may be used to test our model of rupture nucleation.

9. Conclusions

We have shown that relatively simple models of rate-and-state nucleation can quantitatively explain the spatial and temporal evolution of observed nucleating ruptures seen in laboratory experiments. In both laboratory and numerical experiments with a wide range of imposed normal stresses, the nucleation proceeds in two distinct phases: initial slow quasi-static propagation phase and faster acceleration phase, both of which are likely aseismic processes. During the nucleation process, at a given ratio of current rupture length to the critical nucleation length, the product $\Delta \tau^2 V_r$ is approximately constant for a wide range of normal stresses, where $\Delta \tau$ is the stress drop and V_r is the propagation speed of nucleating rupture. Our analysis suggests that the growth of rupture in these laboratory experiments is controlled by the breakdown power density and critical nucleation length. Furthermore, our results highlight the importance of loading conditions in interpreting laboratory observations as the loading rate and configuration significantly affect the propagation speed of nucleating rupture.

The present study demonstrates the utility of advanced physical models to quantitatively interpret the laboratory observations of nucleating shear ruptures. Such an approach—the combination of high-resolution laboratory experiments and numerical modeling—provides a powerful framework for interpreting the nucleation of shear slip events in future laboratory experiments with more complex seismogenic conditions.

References

Ampuero, J.-P., and A. M. Rubin (2008), Earthquake nucleation on rate-and-state faults: Aging and slip laws, *J. Geophys. Res.*, *113*, B01302, doi:10.1029/2007JB005082.

Ben-David, O., S. M. Rubinstein, and J. Fineberg (2010), Slip-stick and the evolution of frictional strength, *Nature*, *463*, 76–79, doi:10.1038/nature08676.

Bouchon, M., H. Karabulut, M. Aktar, S. Özalaybey, J. Schmittbuhl, and M.-P. Bouin (2011), Extended nucleation of the 1999 Mw 7.6 Izmit earthquake, *Science*, *331*(6019), 877–880, doi:10.1126/science.1197341.

Carpenter, B. M., M. M. Scuderi, C. Collettini, and C. Marone (2014), Frictional heterogeneities on carbonate-bearing normal faults: Insights from the Monte Maggio Fault, Italy, *J. Geophys. Res. Solid Earth*, *119*, 9062–9076, doi:10.1002/2014JB011337.

Di Toro, G., R. Han, T. Hirose, N. D. Paola, S. Nielsen, K. Mizoguchi, F. Ferri, M. Cocco, and T. Shimamoto (2011), Fault lubrication during earthquakes, *Nature*, *471*(7339), 494–498.

Dieterich, J. H. (1978), Time-dependent friction and the mechanics of stick-slip, *Pure Appl. Geophys.*, *116*, 790–806, doi:10.1007/BF00876539.

Dieterich, J. H. (1979), Modeling of rock friction: 1. Experimental results and constitutive equations, *J. Geophys. Res.*, *84*, 2161–2168, doi:10.1029/JB084iB05p02161.

Dieterich, J. H. (1992), Earthquake nucleation on faults with rate- and state-dependent strength, *Tectonophysics*, *211*, 115–134, doi:10.1016/0040-1951(92)90055-B.

Dodge, D. A., G. C. Beroza, and W. L. Ellsworth (1996), Detailed observations of California foreshock sequences: Implications for the earthquake initiation process, *J. Geophys. Res.*, *101*(B10), 22,371–22,392.

Fang, Z., J. H. Dieterich, and G. Xu (2010), Effect of initial conditions and loading path on earthquake nucleation, *J. Geophys. Res.*, *115*, B06313, doi:10.1029/2009JB006558.

Freund, L. B. (1998), *Dynamic Fracture Mechanics*, 563 pp., Cambridge Univ. Press, New York.

Geubelle, P. H., and J. R. Rice (1995), A spectral method for three-dimensional elastodynamic fracture problems, *J. Mech. Phys. Solids*, *43*(11), 1791–1824.

Ikari, M. J., A. R. Niemeijer, and C. Marone (2011), The role of fault zone fabric and lithification state on frictional strength, constitutive behavior, and deformation microstructure, *J. Geophys. Res.*, *116*, B08404, doi:10.1029/2011JB008264.

Kaneko, Y., and J.-P. Ampuero (2011), A mechanism for preseismic steady rupture fronts observed in laboratory experiments, *Geophys. Res. Lett.*, *38*, L21307, doi:10.1029/2011GL049953.

Kaneko, Y., and N. Lapusta (2008), Variability of earthquake nucleation in continuum models of rate-and-state faults and implications for aftershock rates, *J. Geophys. Res.*, *113*, B12312, doi:10.1029/2007JB005154.

Kaneko, Y., N. Lapusta, and J.-P. Ampuero (2008), Spectral element modeling of spontaneous earthquake rupture on rate and state faults: Effect of velocity-strengthening friction at shallow depths, *J. Geophys. Res.*, *113*, B09317, doi:10.1029/2007JB005553.

Kaneko, Y., J.-P. Ampuero, and N. Lapusta (2011), Spectral-element simulations of long-term fault slip: Effect of low-rigidity layers on earthquake-cycle dynamics, *J. Geophys. Res.*, *116*, B10313, doi:10.1029/2011JB008395.

Kato, N., and T. Hirasawa (1996), Effects of strain rate and strength nonuniformity on the slip nucleation process: A numerical experiment, *Tectonophysics*, *265*(3), 299–311.

Kato, N., and T. E. Tullis (2001), A composite rate- and state-dependent law for rock friction, *Geophys. Res. Lett.*, *28*(6), 1103–1106.

Kato, N., K. Yamamoto, H. Yamamoto, and T. Hirasawa (1992), Strain-rate effect on frictional strength and the slip nucleation process, *Tectonophysics*, *211*(1), 269–282.

Lapusta, N., and Y. Liu (2009), Three-dimensional boundary integral modeling of spontaneous earthquake sequences and aseismic slip, *J. Geophys. Res.*, *114*, B09303, doi:10.1029/2008JB005934.

Lapusta, N., and J. R. Rice (2003), Nucleation and early seismic propagation of small and large events in a crustal earthquake model, *J. Geophys. Res.*, *108*(B4), 2205, doi:10.1029/2001JB000793.

Latour, S., A. Schubnel, S. Nielsen, R. Madariaga, and S. Vinciguerra (2013), Characterization of nucleation during laboratory earthquakes, *Geophys. Res. Lett.*, *40*, 5064–5069, doi:10.1002/grl.50974.

Lawn, B. (1993), *Fracture of Brittle Solids—Second Edition*, 378 pp., Cambridge Univ. Press, Cambridge, U. K.

Liu, Y., and N. Lapusta (2008), Transition of mode II cracks from sub-Rayleigh to intersonic speeds in the presence of favorable heterogeneity, *J. Mech. Phys. Solids*, *56*, 25–50.

Liu, Y., and J. R. Rice (2005), Aseismic slip transients emerge spontaneously in three-dimensional rate and state modeling of subduction earehquake sequences, *J. Geophys. Res.*, *110*, B08307, doi:10.1029/2004JB003424.

Marone, C. (1998), Laboratory-derived friction laws and their application to seismic faulting, *Annu. Rev. Earth Planet. Sci.*, *26*, 643–696, doi:10.1146/annurev.earth.26.1.643.

McGuire, J. J., M. Boettcher, and T. H. Jordan (2005), Foreshock sequences and earthquake predictability on East Pacific Rise transform faults, *Nature*, *434*, 457–461, doi:10.1038/nature03377.

McLaskey, G. C., and B. D. Kilgore (2013), Foreshocks during the nucleation of stick-slip instability, *J. Geophys. Res. Solid Earth*, *118*, 2982–2997, doi:10.1002/jgrb.50232.

Nagata, K., M. Nakatani, and S. Yoshida (2012), A revised rate-and state-dependent friction law obtained by constraining constitutive and evolution laws separately with laboratory data, *J. Geophys. Res.*, *117*, B02314, doi:10.1029/2011JB008818.

Nielsen, S., J. Taddeucci, and S. Vinciguerra (2010), Experimental observation of stick-slip instability fronts, *Geophys. J. Int.*, *180*, 697–702, doi:10.1111/j.1365-246X.2009.0444.x.

Noda, H., M. Nakatani, and T. Hori (2013), Large nucleation before large earthquakes is sometimes skipped due to cascade-up—Implications from a rate and state simulation of faults with hierarchical asperities, *J. Geophys. Res. Solid Earth*, *118*, 2924–2952, doi:10.1002/jgrb.50211.

Ohnaka, M. (1996), Nonuniformity of the constitutive law parameters for shear rupture and quasistatic nucleation to dynamic rupture: A physical model of earthquake generation processes, *Proc. Natl. Acad. Sci. U.S.A.*, *93*(9), 3795–3802.

Ohnaka, M., and Y. Kuwahara (1990), Characteristic features of local breakdown near a crack-tip in the transition zone from nucleation to unstable rupture during stick-slip shear failure, *Tectonophysics*, *175*(1), 197–220.

Okubo, P. G., and J. H. Dieterich (1984), Effects of physical fault properties on frictional instabilities produced on simulated faults, *J. Geophys. Res.*, *89*(B7), 5817–5827.

Radiguet, M., D. S. Kammer, and J.-F. Molinari (2015), The role of viscoelasticity on heterogeneous stress fields at frictional interfaces, *Mech. Mater.*, *80*, 276–287, doi:10.1016/j.mechmat.2014.03.009.

Rathbun, A. P., and C. Marone (2013), Symmetry and the critical slip distance in rate and state friction laws, *J. Geophys. Res. Solid Earth*, *118*, 3728–3741, doi:10.1002/jgrb.50224.

Rice, J. R. (1993), Spatio-temporal complexity of slip on a fault, *J. Geophys. Res.*, *98*(B6), 9885–9907, doi:10.1029/93JB00191.

Rubin, A. M. (2008), Episodic slow slip events and rate-and-state friction, *J. Geophys. Res.*, *113*, B11414, doi:10.1029/2008JB005642.

Rubin, A. M., and J.-P. Ampuero (2005), Earthquake nucleation on (aging) rate and state faults, *J. Geophys. Res.*, *110*, B11312, doi:10.1029/2005JB003686.

Ruina, A. L. (1983), Slip instability and state variable friction laws, *J. Geophys. Res.*, *88*, 10,359–10,370, doi:10.1029/JB088iB12p10359.

Schmitt, S. V., P. Segall, and T. Matsuzawa (2011), Shear heating-induced thermal pressurization during earthquake nucleation, *J. Geophys. Res.*, *116*, B06308, doi:10.1029/2010JB008035.

Scholz, C. H. (2002), *The Mechanics of Earthquakes and Faulting*, 2nd ed., 496 pp., Cambidge Univ. Press, New York.

Schurr, B., et al. (2014), Gradual unlocking of plate boundary controlled initiation of the 2014 Iquique earthquake, *Nautre*, *512*(7514), 299–302.

Svetlizky, I., and J. Fineberg (2014), Classical shear cracks drive the onset of dry frictional motion, *Nature*, *509*(7499), 205–208, doi:10.1038/nature13202.

Tape, C., M. West, V. Silwal, and N. Ruppert (2013), Earthquake nucleation and triggering on an optimally oriented fault, *Earth Planet. Sci. Lett.*, *363*, 231–241.

Trømborg, J. K., H. A. Sveinsson, J. T. Scheibert, K. Thøgersen, D. S. Amundsen, and A. Malthe-Sørenssen (2014), Slow slip and the transition from fast to slow fronts in the rupture of frictional interfaces, *Proc. Natl. Acad. Sci. U.S.A.*, *111*(24), 8764–8769.

Tullis, T. E. (1996), Rock friction and its implications for earthquake prediction examined via models of Parkfield earthquakes, *Proc. Natl. Acad. Sci. U.S.A.*, *93*(9), 3803–3810.

Wei, M., Y. Kaneko, Y. Liu, and J. J. McGuire (2013), Episodic fault creep events in California controlled by shallow frictional heterogeneity, *Nat. Geosci.*, *6*, 566–570, doi:10.1038/ngeo1835.

Yabe, Y., M. Nakatani, M. Naoi, J. Philipp, C. Janssen, T. Watanabe, T. Katsura, H. Kawakata, G. Dresen, and H. Ogasawara (2015), Nucleation process of an M2 earthquake in a deep gold mine in South Africa inferred from on-fault foreshock activity, *J. Geophys. Res. Solid Earth*, *120*, 5574–5594, doi:10.1002/2014JB011680.